JOURNAL OF GEOPHYSICAL RESEARCH, VOL. 114, B06310, doi:10.1029/2008JB006119, 2009

Crustal structure of Deception Island volcano from *P* wave seismic tomography: Tectonic and volcanic implications

Daria Zandomeneghi,[1,2] Andrew Barclay,[3] Javier Almendros,[1,4] Jesús M. Ibañez Godoy,[1,4] William S. D. Wilcock,[5] and Tami Ben-Zvi[5]

Received 25 September 2008; revised 20 March 2009; accepted 9 April 2009; published 19 June 2009.

[1] Deception Island (62°59′S, 60°41′W) is an active volcano located in the Bransfield Strait between the Antarctic Peninsula and the South Shetland Islands. The island is composed of rocks that date from <0.75 Ma to historical eruptions (1842, 1967, 1969, and 1970), and nowadays most of its activity is represented by vigorous hydrothermal circulation, slight resurgence of the inner bay floor, and intense seismicity, with frequent volcano-tectonic and long-period events. In January 2005 an extensive seismic survey took place in and around the island to collect high-quality data for a high-resolution *P* wave velocity tomography study. A total of 95 land and 14 ocean bottom seismometers were deployed, and more than 6600 air gun shots were fired. As a result of this experiment, more than 70,000 travel time data were used to obtain the velocity model, which resolves strong *P* wave velocity contrasts down to 5 km depth. The joint interpretation of the Vp distribution together with the results of geological, geochemical, and other geophysical (magnetic and gravimetric) measurements allows us to map and interpret several volcanic features of the island and surroundings. The most striking feature is the low *P* wave velocity beneath the caldera floor which represents the seismic image of an extensive region of magma beneath a sediment-filled basin. Another low-velocity zone to the east of Deception Island corresponds to seafloor sedimentary deposits, while high velocities to the northwest are interpreted as the crystalline basement of the South Shetland Islands platform. In general, in the tomographic image we observe NE-SW and NW-SE distributions of velocity contrasts that are compatible with the regional tectonic directions and suggest that the volcanic evolution of Deception Island is strongly conditioned by the Bransfield Basin geodynamics.

Citation: Zandomeneghi, D., A. Barclay, J. Almendros, J. M. Ibañez Godoy, W. S. D. Wilcock, and T. Ben-Zvi (2009), Crustal structure of Deception Island volcano from *P* wave seismic tomography: Tectonic and volcanic implications, *J. Geophys. Res.*, *114*, B06310, doi:10.1029/2008JB006119.

1. Introduction

[2] Deception Island is an example of a subaerial volcano in an extensional back-arc environment. It is situated between the South Shetland Islands (SSI) and the Antarctic Peninsula in the Bransfield basin, a NE-SW trending marginal basin that is 400 km long and 60 km wide (Figure 1). The Bransfield Basin can be morphologically divided into three subbasins; Deception Island is located at the western limit of the Central Bransfield Basin (CBB) [*Gordon and Nowlin*, 1978].

[3] The Pacific margin of the Antarctic Peninsula was an active plate boundary during the Mesozoic and Cenozoic, when the oceanic Phoenix Plate was subducting below the Antarctic Peninsula toward the ESE. When spreading at the Aluk Ridge NW of the SSI slowed, at about 4 Ma [*Christeson et al.*, 2003], rollback of the descending slab began, leading to an extensional regime in the Bransfield Strait. Although there is no well defined Wadati-Benioff zone, the slow subduction of the former Phoenix plate continues today [*Pelayo and Wiens*, 1989]. The subduction rate is probably similar to the opening rate of the Bransfield Strait, which is estimated from GPS measurements at ∼10 mm/a [*Robertson-Maurice et al.*, 2003; *Vuan et al.*, 2005].

[4] A major left-lateral strike-slip plate boundary is also present between the Antarctic and Scotia plates, along the South Scotia Ridge (Figure 1). Resulting transtension may be competing with slab rollback as the principal driving mechanism for the extension, NE to SW propagating, at the East Bransfield Basin [*Galindo-Zaldivar et al.*, 1996;

[1]Instituto Andaluz de Geofísica, University of Granada, Granada, Spain.
[2]Now at Department of Earth and Environmental Science, New Mexico Institute of Mining and Technology, Socorro, New Mexico, USA.
[3]Lamont-Doherty Earth Observatory, Earth Institute at Columbia University, Palisades, New York, USA.
[4]Also at Departamento de Física Teórica y del Cosmos, University of Granada, Granada, Spain.
[5]School of Oceanography, University of Washington, Seattle, Washington, USA.

0148-0227/09/2008JB006119$09.00

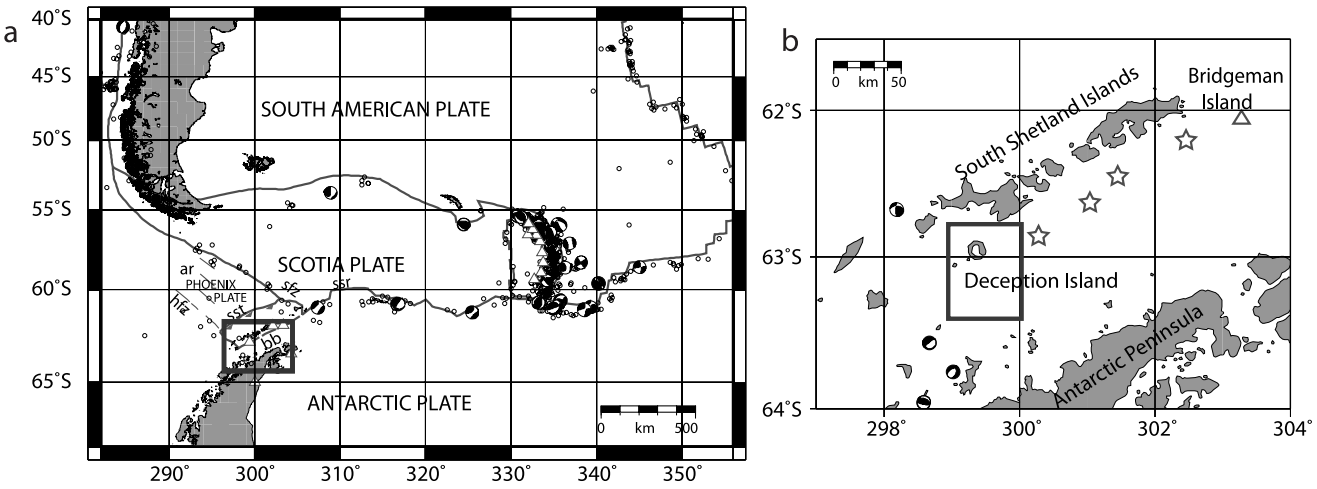

Figure 1. Location of Deception Island. (a) Regional map showing plate boundaries (thick lines) [*Bird*, 2003] and focal mechanisms for Mw > 6.5 earthquakes from the Harvard and NEIC database (1976–2008). Abbreviations are as follows: bb, Bransfield Basin; ssr, South Scotia Ridge; sfz, Shackleton Fracture Zone; sst, South Shetland Trench; hfz, Hero Fracture Zone; ar, Aluk Ridge. The box shows the location of Figure 1b; triangles are known active volcanoes from the Global Volcanism Program database. (b) Bransfield Basin region. Stars are seafloor volcanic centers. The box shows the location of Figure 2.

Klepeis and Lawer, 1996; *Lawver et al.*, 1996; *Maestro et al.*, 2007; *Rey et al.*, 1995; *Robertson-Maurice et al.*, 2003].

[5] The CBB has a broad neovolcanic zone of seamounts and volcanic ridges along its axis, but despite the evidence of considerable NW-SE directed extension, seafloor spreading has not yet initiated [*Christeson et al.*, 2003; *Lawver et al.*, 1996]. Between the neovolcanic zone and the SSI there are large NW-SE trending normal faults that control the extension of several depocenters in a direction that is normal to the basin extension and with a strike-slip component that offsets the neovolcanic zone toward the South Shetland margin [*Barker and Austin*, 1998; *Christeson et al.*, 2003; *Gracia et al.*, 1996; *Prieto et al.*, 1998].

[6] The origin, history, and regional tectonic context of Deception Island are poorly understood. Although some models propose that Deception Island may have experienced a major caldera-forming eruption, it has also been suggested that the inner flooded bay (Port Foster) formed progressively by passive extension along sets of normal faults that cut the island [*Marti et al.*, 1996; *Smellie et al.*, 2002]. Structural mapping and seismic reflection studies within Port Foster show that the local tectonics is strongly controlled by two major fault systems. A NE-SW striking system is consistent with the regional extensional regime of the Bransfield Strait and controls the alignment of the eruptive centers of 1967 and 1970 [*De Rosa et al.*, 1995]. The second system is observed in fault orientations and strikes NNW-SSE, approximately perpendicular to the first one [*Paredes et al.*, 2006]. This system may control the shape of Costa Recta, the eastern coast of Deception Island [*Fernandez-Ibañez et al.*, 2005; *Maestro et al.*, 2007].

[7] The action of extensional processes on Deception Island is confirmed by the regional deformation component in the GPS measurements [*Dietrich et al.*, 2001; *Robertson-Maurice et al.*, 2003]. Studies of the deformation field local to Deception Island [*Ramirez-Rodriguez*, 2006] during the last few years, have shown contemporaneous action of the two fault systems. In addition, the floor of the northern sector of Port Foster has been uplifting at a rate of 0.3–0.5 m/y and has been attributed to inflation of a shallow magma chamber and a high rate of sedimentation [*Cooper et al.*, 1999]. The presence of melt beneath Port Foster has also been inferred from seismic refraction studies [*Somoza et al.*, 2004; *Ben-Zvi et al.*, 2007], gravity, magnetism and seismic attenuation observations [*Catalan et al.*, 2006; *Muñoz-Martin et al.*, 2005; *Vila et al.*, 1995]. There have been six documented volcanic eruptions at Deception Island between 1841 and 1971 [*Simkin and Siebert*, 2002], all located around Port Foster, although present-day activity is limited to fumaroles and hot sands.

[8] The local seismicity of Deception Island is consistent with that of an active and deforming volcano. It includes volcano-tectonic earthquakes (VT), long-period events (LP), tremor, hybrid events, avalanche signals, rockfalls and ice cracks [*Alguacil et al.*, 1999; *Almendros et al.*, 1997; *Ibañez et al.*, 2000]. The VT activity is relatively low level and composed of small events that are highly clustered in time and space and mainly associated with the main fractures of the island. They mostly show normal mechanism and near-vertical fault planes [*Vila et al.*, 1995]. In 1992 and 1999 intense swarms took place along alignments approximately parallel to the major fault systems of the island, including those in a NE-SW direction [*Almendros et al.*, 2004; *Ibañez et al.*, 2003; *Ortiz*, 1997]. Intense long-period activity, observed using seismic antennas, has been recognized throughout the island and is differentiated into three groups, depending on duration and frequency content (LP, tremor, and hybrid events) [*Alguacil et al.*, 1999; *Ibañez et al.*, 2000]. The LP seismicity [*Chouet*, 2003] on Deception Island has been attributed to the interaction of shallow aquifers with high-temperature rocks where resonances in cracks are excited by exploding or imploding steam bubbles [*Almendros et al.*, 1997]. This mechanism also explains the hybrid earthquakes that are LP events but

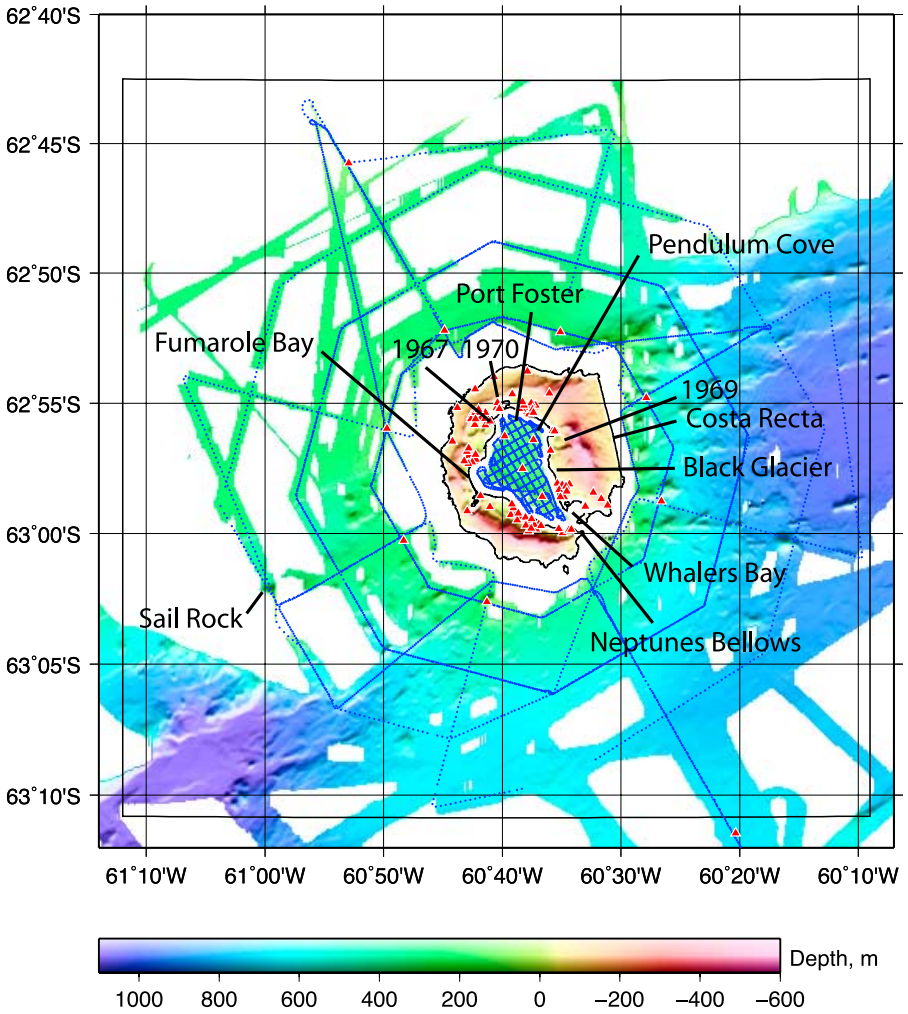

Figure 2. Configuration of seismic tomography experiment. Land and ocean bottom seismometers are shown by triangles; circles are individual shot locations. Toponyms and historical eruption centers are indicated. Island topography and seafloor bathymetry are from *Barclay et al.* [2009].

with an impulsive onset. Many of the VT events have similar locations to the hybrid events and this has been attributed to the same fluids lubricating faults [*Ibañez et al.*, 2003].

[9] The oldest rocks on Deception Island date from <0.75 Ma, although exposure is poor [*Keller et al.*, 2002]. Rock compositions vary from basaltic to dacitic, and show a wide range even within single, small pyroclastic eruptions. On a TAS (Total Alkali-Silica) diagram, they are generally located between the alkaline and subalkaline suites, high in Na_2O/K_2O, and although this range is similar to that of MORB, other element contents suggest affinity to island arc tholeiites and even back-arc basin basalts. The element variations are consistent with low-pressure crystal fractionation and evolution in an open system with an external source influence or periodic replenishment from depth, as for example in an upper crustal magma chamber where mafic melt that is continuously fractionating interacts with small batches of fresh magma, possibly triggered by the regional extensional tectonics. Two main eruptive styles have been recognized in the historical activity of Deception Island [*De Rosa et al.*, 1995]: (1) magmatic strombolian explosions (1842, 1969, first phase of 1967 eruption) and (2) phreatomagmatic eruptions along regional fault systems, involving the interaction of water from ice or the ocean leading to surtseyan type eruptions (1967), or phreatomagmatic explosions (1970). These historical eruptions have renewed the scientific interest in the island's volcanic activity and risk potential, and since 1989 the Spanish and Argentinian governments have maintained bases on the island, from which scientific investigations are supported each summer.

[10] The understanding of Deception Island volcano is severely limited by the incomplete knowledge of its internal structure. There have been many studies of its evolution and present-day state (e.g., British Antarctic Survey Monograph [*Smellie et al.*, 2002]) which all indicate a complex history that has been strongly influenced by both magmatic and tectonic processes. However, without information on the distribution of melt, the depth of sediments and the location of intrusive bodies and fault zones beneath and around the island, the models for the structure and evolution of Deception Island are poorly constrained.

[11] A three-dimensional (3-D) seismic *P* wave tomography survey of Deception Island volcano was conducted as part of the TOMODEC project in January 2005. In this paper,

we describe the seismic experiment, the collection and analysis of the data, the tomographic inversion and its application. We present an image of seismic velocity structure for Deception Island and its surroundings. This analysis follows the two-dimensional (2-D) tomographic models obtained along two orthogonal profiles with a similar data set from the same experiment [*Ben-Zvi et al.*, 2009].

[12] The main aims of this work are to understand the distribution of melt in the shallow crust, to relate the tomographic images to other geophysical and geological observations from Deception Island and to test existing ideas for the structure and evolution of the volcano in the context of regional tectonics.

2. Seismic Tomography Experiment

[13] The seismic experiment was designed to obtain a three-dimensional seismic image of the volcano and its surrounding region. The particular geometry of the island with the flooded inner bay allowed for a unique and elaborate seismic experiment, with seismometers deployed on land and on the seafloor within a 54 $\times$ 80 km^2 area centered on Deception Island (Figure 2). This seismometer network was used to record more than 6600 air gun shots that were located both inside Port Foster and around the island from the R/V *Hesperides* during a 2-week period. In the interior of Port Foster, the tracks comprised a dense grid of perpendicular lines with a spacing of 500 m and with shots located every 120 m along each line. Outside the island, shots were fired with along-track spacings of 170 and 340 m in three main configurations: (1) two straight lines, one 92 km long and oriented NNW-SSE, and the other 55 km long in a WSW-ENE direction [*Ben-Zvi et al.*, 2007]; (2) three concentric polygons at distances of 10, 15 and 20 km from the center of the island; and (3) radial lines with orientations spaced 45° apart that were used to minimize gaps in shot coverage. The shot pattern was modified as a result of navigational constraints including shoals and sea ice. Approximately 580 km of air gun shot lines were completed.

[14] The receiver network consisted of 122 land and 14 ocean bottom seismometer locations. This coverage was obtained by relocating 27 stations and then repeating the shooting in a very similar pattern, in order to improve the receiver coverage. The OBSs were distributed in the inner bay and in a circular configuration around the island; an additional deployment of OBSs along the outermost shot track failed because of a software fault. The land seismic stations were installed at least 0.2 km apart across the island, and included autonomous stations as well as dense (110 m average spacing among sensors) and sparse (620 m average spacing) seismometer arrays. The distribution of most of the land stations was constrained by cliffs, glaciers, and lakes and was limited to accessible sites.

[15] Each OBS was equipped with a broadband three-component seismometer [*Webb*, 1998] and a broadband hydrophone that were sampled continuously at 125 Hz. The position and depth of each of the OBSs were determined by inverting water path travel times for nearby shots [*Creager and Dorman*, 1982]. The land seismic stations used short period (1 Hz) sensors except for seven locations where M24 seismometers with 20 s Lennartz sensors were deployed. All land seismometers recorded continuously with a sampling rate of 125 Hz or 100 Hz depending on the station type. Thirty of the land sites were instrumented with three-component sensors. A total of 120 Gb of seismic data were collected, in addition to gravity, magnetic and multibeam bathymetry data that were acquired along the same ship tracks [*Barclay et al.*, 2009].

3. Data

[16] The quality of data recorded during the seismic experiment was good, with clearly identifiable and pickable *P* wave first arrivals observed both on land and ocean bottom seismometer records out to 40 km range. Noise levels were noticeably higher during storms because of strong wind and wave action. Waveforms of crustal phases with similar raypaths consistently showed strong variability in their shapes, which we attributed to variable water paths or closely spaced near-source or near-receiver attenuating heterogeneities (Figure 3). Many of the arrivals were considerably reverberatory as a result of the air gun bubble pulse and reverberation in the water column. All of the arrivals were assumed to be crustal phases because, in our starting one-dimensional (1-D) velocity model, a maximum source-receiver offset of 40 km corresponds to a maximum turning depth of about 5 km below the seafloor for *P* wave refracted arrivals, and the shallowest estimate for Moho depth around Deception Island is around 15 km [*Christeson et al.*, 2003].

[17] The final data set consists of travel times for more than 70,000 *P* wave first arrivals. These arrivals were identified on record sections and were picked and assigned uncertainties using a combination of manual and automatic picking approaches. An automatic picking algorithm based on the ration of the average signal energy in a short and long data window (Seismic Analysis Code routine APK [*Goldstein et al.*, 2003]) was applied to the records after high-pass filtering at 5 Hz. These automatic picks were then plotted on trace gathers and verified and adjusted manually as necessary. Each station recorded $\sim$1500 pickable shots on average, and each shot was picked on at least 15 stations.

4. Tomographic Inversion Method

[18] The *P* wave travel times were inverted for the 3-D velocity model of Deception Island and the surrounding region using the seismic tomography code of *Toomey et al.* [1994]. This method, which uses shortest-time ray tracing and LSQR algorithm inversion [*Paige and Saunders*, 1982], has been applied to a number of local active source seismic tomography experiments at mid-ocean ridges [*Barclay et al.*, 1998; *Barclay and Wilcock*, 2004; *Dunn et al.*, 2001; *Tian et al.*, 2000; *Toomey et al.*, 1998, 2007].

[19] In this method, approximate raypaths and travel times are calculated from each point on a 3-D grid to each station using the shortest-path algorithm [*Moser*, 1991]. Because it can include diffracted rays, the shortest-time ray tracing approach is particularly appropriate for the sharp slowness contrasts and low-velocity regions that are typical of active volcanic regions. Topography is taken into account

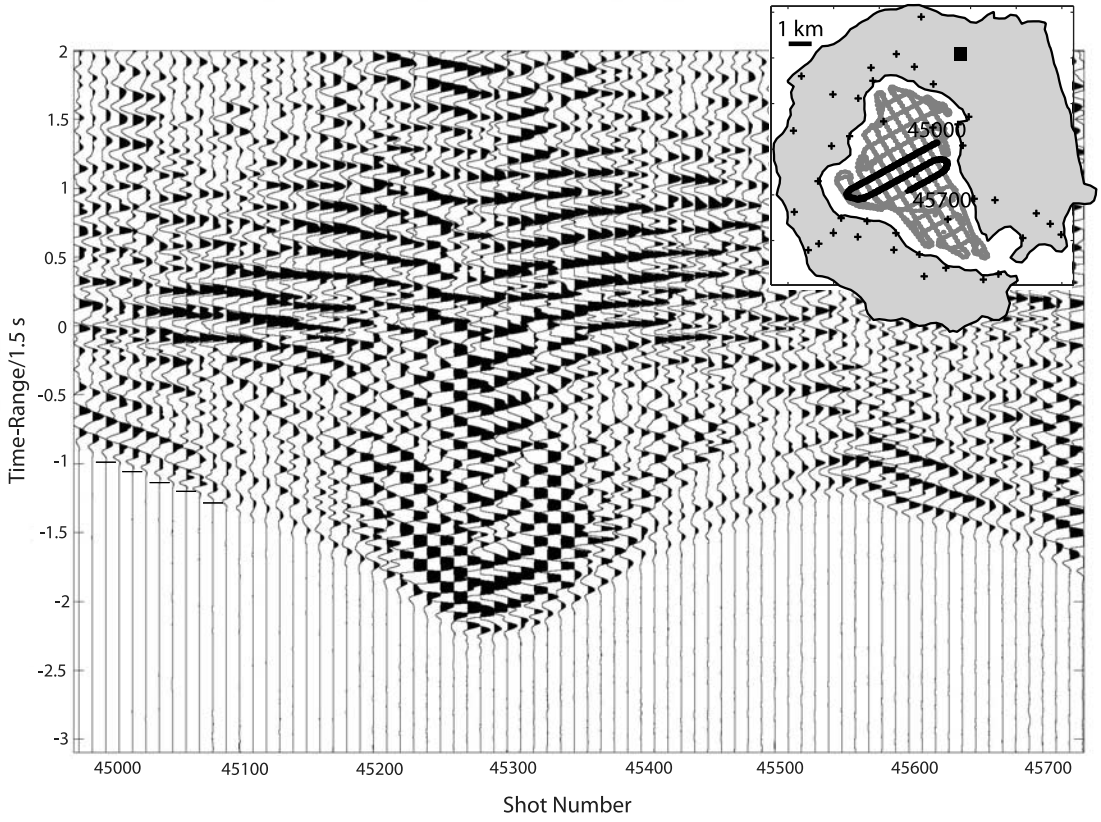

Figure 3. Example record section for shots within Port Foster, recorded on an inner bay seismometer. (See inset: black circles indicate shot locations, with shot numbers of the section endpoints. Black square is the station position, and other seismometer locations are indicated by crosses.) Reduction velocity is 1.5 km/s.

by shearing each column of grid nodes vertically, following the seafloor bathymetry and island topography. This was necessary for the Deception Island experiment because the seismometer locations were in Port Foster and on and around the island and the model elevation ranged from a maximum height of 500 m to a maximum depth of 750 m [*Barclay et al.*, 2009].

[20] The perturbation model parameters are defined on a collocated 3-D grid that is typically sparser than the ray tracing grid. The regularization of the inverse problem is primarily controlled by damping and smoothing weights and lengths [*Toomey et al.*, 1994], and determining their appropriate values is a trial and error approach. We searched for the values of both damping and smoothing that simultaneously minimized the root-mean-squared (RMS) travel time error and perturbations made to the starting slowness structure. The optimum parameters were chosen from visual inspection, aided by inversions of synthetic data sets, to test for the introduction of artifacts. The final regularization values were: half-length for smoothing $\tau_x = \tau_y = \tau_z = 1.1$ km (for the sparse grid; see below) and 0.8 km (for the dense grid); damping $\lambda_p = 100$; horizontal and vertical smoothing $\lambda_v = \lambda_h = 30$ (for the sparse grid) and 20 (for the dense).

[21] The accuracy of the shortest-path ray tracing method depends primarily on the spacing of the ray tracing grid, which is however limited by the computation time required. The large area covered by the Deception Island experiment meant that the tradeoff between accuracy and computation time was significant. We chose to consider two parameterized different models: a large, sparse grid that was centered on Deception Island and extended 53 $\times$ 52 $\times$ 12 km in the E-W, N-S directions and depth, respectively, and a smaller model that included the region around Port Foster and extended 12 $\times$ 14 $\times$ 7 km. The large, sparse model space had a ray tracing grid spacing of 250 m and a perturbational grid spacing of 500 m; corresponding values for the small, dense model were 100 m and 200 m, respectively. Using the dense spacing for the entire experiment area would have been computationally infeasible; however by comparing the results for the region within Port Foster for both cases, we established that the appearance of the tomographic images was similar, and that the large,

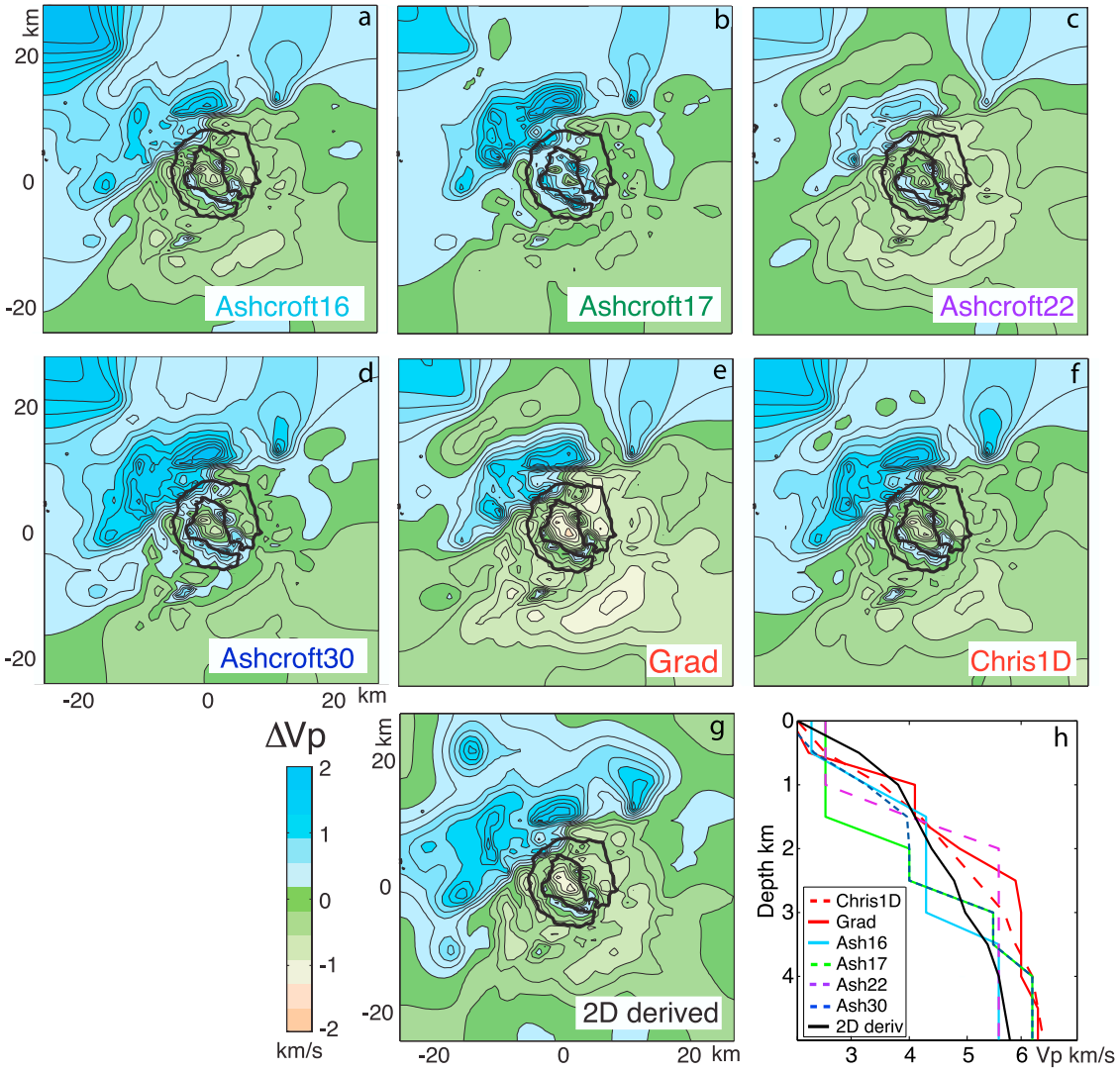

Figure 4. Selection of the starting model. (a–g) Three-dimensional tomographic images at 1 km depth obtained for the full data set and using different starting models. In each case, perturbations to the individual starting model are shown. The coast of Deception Island is outlined in black. (h) Averaged 1-D velocity models for each final model of Figures 4a–4g. Absolute *P* wave velocities are shown. See text for details.

sparse model was acceptable. However, the small, dense image was more detailed, and we therefore obtained separate tomographic images for the Port Foster region.

[22] In order to assess the goodness of fit of a given slowness model to the travel time data, it is vital to know how much of the data variance can be attributed to stochastic processes, as opposed to unknown seismic structure. Following the approach of *Barclay et al.* [1998], we concluded that the expected error in the travel times was dominated by the RMS picking error, which we estimated to be ~11 ms.

4.1. One-Dimensional Inversions and Starting Model

[23] An appropriate starting model is required to produce a valid linearization of the inverse problem, and hence to produce an accurate result. We tested seven starting models taken from previous experiments in the region [*Ashcroft*, 1972; *Christeson et al.*, 2003; *Grad et al.*, 1992, 1997] and from the 1-D average (called "2-D derived") of two 2-D velocity profiles that were also derived from the TOMODEC data set [*Ben-Zvi et al.*, 2009, also presented paper, 2007]. We used each of them to invert our data for a 3-D velocity structure, and then we compared their averaged to 1-D results (Figure 4). All seven starting models converged to the same basic pattern of primary anomalies within our region of resolution (the high-velocity anomaly in the NW sector of the island and the low-velocity perturbation in the inner bay), but the absolute value of the anomalies and of some smaller secondary features is slightly dependent on the starting model. We selected "2-D derived" as the starting model because it resulted in stable inversions and gave the best fit to the data.

4.2. Resolution

[24] The accuracy and resolution of the tomographic velocity model are affected by uncertainties in travel time picks, limitations in the method, an uneven ray distribution and the model parameterization. While the effects of

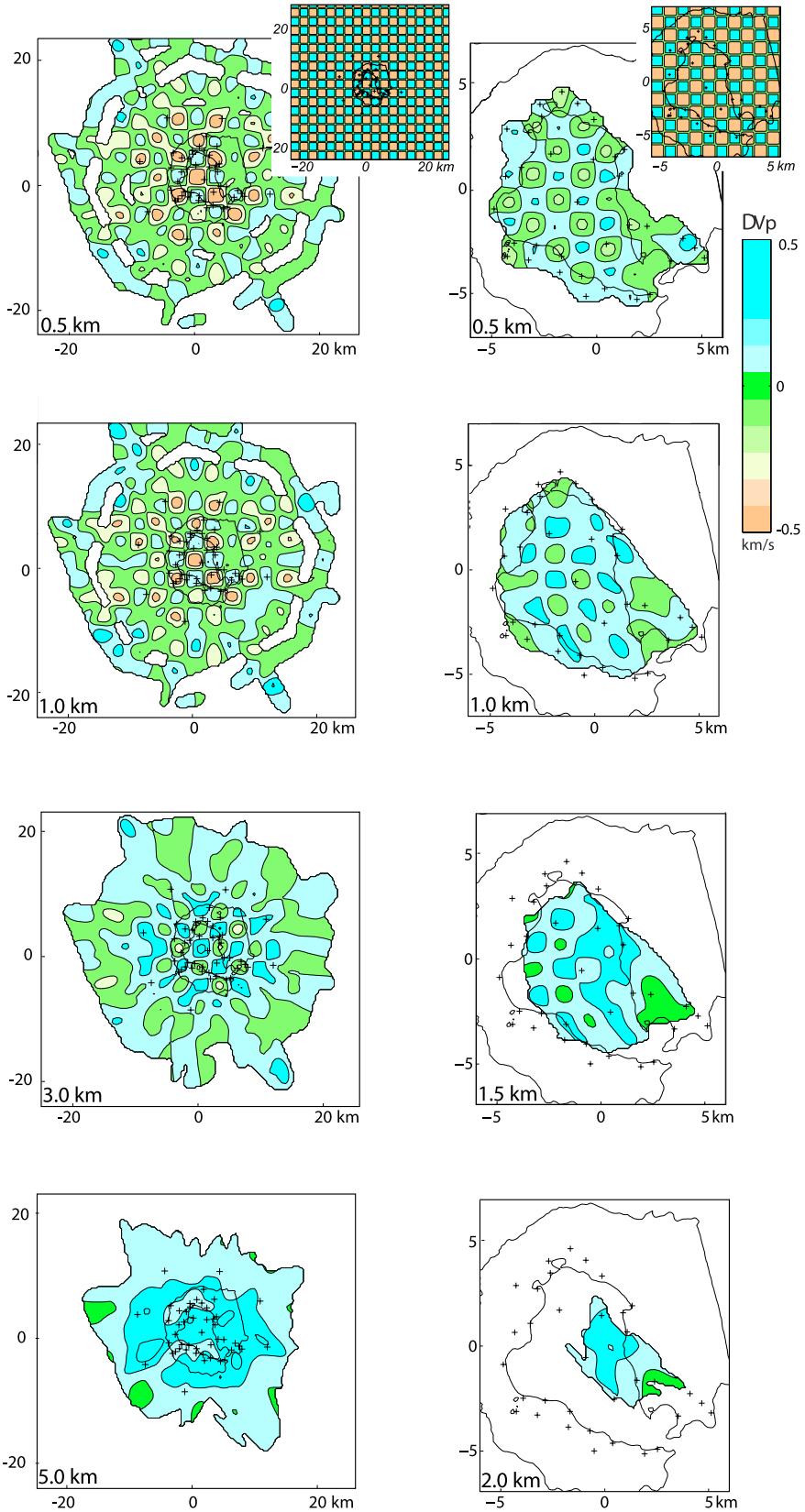

Figure 5. Results of synthetic checkerboard tests for the (left) sparse and (right) dense inversions. The magnitude and pattern of the starting anomalies are shown at the top (the anomaly intensity sense varies depending on the depth, but the pattern is maintained). Contour interval is 0.2 km/s. The coast of Deception Island is outlined in black, and the crosses are seismometer locations. Areas with zero or low ray coverage are not shown. Horizontal slices are at depths indicated in each plot.

reduced resolution include underestimated amplitudes and smoothing, the most critical consequence is the generation of artifacts in the image that are interpreted as real features. We used a number of methods to assess the reliability of the velocity features in the tomographic image including evaluation of ray coverage and recovery tests for a variety of synthetic velocity structures. For the recovery tests, we calculated travel times for the experimental source and receiver distributions through a variety of synthetic velocity models that included 3-D checkerboard patterns, isolated spikes, and test anomalies, including a synthetic structure identical to the final result of the inversion. We added random noise to the synthetic travel times, and then inverted them using the same parameters as were used for the true inversion. The location and intensity of the recovered features then provided a measure of the resolution of the inversion and of the reliability of the final tomographic structure.

[25] Results for the checkerboard tests are shown in Figure 5. Cuboids of 10% alternating positive and negative velocity perturbations with horizontal lengths of 3 × 3 km and thickness 2 km were added to the initial 1-D model for the sparse inversion, and 1 × 1 × 1 km for the dense inversion. These anomalies were smoothed along all three dimensions. The 10% variation we chose is large enough to provide a perturbation greater than that expected from a noise level equivalent to the final RMS but also small enough to minimize the deviation of raypaths from those in the final model [*Evangelidis et al.*, 2004].

[26] The checkerboard test for the sparse inversion shows very good recovery of the anomalies beneath Port Foster and the western half of Deception Island that decreases with depth to ∼5 km depth. The eastern section of Deception Island was ice covered and had few seismometers, and this limited the ray coverage. The anomaly pattern is also recognizable around Deception Island, although it degrades with both depth and distance from the island. There are no significant artifacts in the image, except for an overall region of positive anomaly that appears in the center of the model at depths greater than 3 km (Figure 5). We attribute this effect to a tradeoff between maximum depth and velocity for the deepest-diving rays. For the dense inversion centered on Port Foster, the recovery of the checkerboard pattern is excellent to ∼2 km depth, but rapidly degrades below that depth. The high resolution is due to the very high density of raypaths, while the shallow depth and restricted lateral extent of the recovered image is because only shots and receivers within and around Port Foster were used.

5. Results

[27] As a result of computational limitations, tomographic inversions using two separate grid configurations were produced: a sparse grid that encompassed all of the shots and receivers, and a denser, smaller grid that included Port Foster and its shoreline. Convergence of the tomographic inversion for the sparse grid was obtained after 6 iterations of ray tracing and inversion, when the RMS data misfit was reduced from 247 ms for the 1-D starting model to 52 ms (with a variance reduction of 95%). For the denser grid, the inversion result was also stable after 6 ray tracing iterations, with a RMS decrease from 260 ms to 34 ms (variance reduction of 98%). Results from both grid configurations were used to image the overall velocity structure of Deception Island and surrounding region (Figure 6). The resulting structure is strongly heterogeneous with a lateral variation of >2 km/s between the surface and 5 km depth, for both grid configurations, as is typical of volcanic regions [*Lees*, 2007].

[28] Several pronounced anomalies are present in the seismic structure in areas that the synthetic tests indicate are well resolved (see section 4.2.). We observe a wide high-velocity region that dominates to the NW of Deception Island (A1), present between the surface and 5.5 km depth and which has a sharp, linear SE boundary. This perturbation is not laterally homogeneous and contains three maxima that appear to be associated with local perturbations. Other smaller high-velocity anomalies are recognizable in the model, including a horseshoe-shaped anomaly that wraps around the southern shore of Port Foster (A2), an anomaly directly to the south of Deception Island (A3) and an anomaly centered ∼12 km SW of Deception Island that coincides with the position of Sail Rock, an isolated 40-m-high sea stack (A4).

[29] Low-velocity regions are also present. The most pronounced is the anomaly that lies beneath Port Foster (B1), and extends throughout the entire resolved volume from 0 to 5.5 km depth. Its maximum strength is reached at 1 km depth and maintained until at least 3.5 km, and below it appears to decrease, together with resolution. We used the solution for the denser grid inversion to image the Port Foster shallow velocity structure in more detail. The shape and intensity of the B1 low-velocity anomaly change between the surface and 1.5 km depth. At shallowest depths (0–0.5 km) the anomaly includes several local maxima located in correspondence of the 1967 and 1970 eruption centers, in front of Black Glacier, and Fumarole Bay. At greater depth, these coalesce into a single maximum and the low-velocity volume has an overall NW-SE elongation, with sharp and relatively linear boundaries. Other low velocities appear to the E and SE of the island (B2), with an overall irregular shape although there is a slight correspondence at 0.5 km depth with the location of Costa Recta. A third prominent low-velocity anomaly is observed to the SW of Deception Island (B3).

6. Interpretation

[30] Lateral *P* wave velocity variations in the upper crust of a volcanically and tectonically active environment such as Deception Island may be due to a range of processes that include: the juxtaposition of different rock types (e.g., sediments of different origin, magmatic intrusives and extrusives); density-porosity variations, fracturing and geochemical alteration; anisotropic distribution of their properties, temperature differences and the presence of fluids (melt or water) [*Bonner et al.*, 1998; *Christensen*, 1996; *Fehler et al.*, 1998; *Lees and Wu*, 2000; *Mavko*, 1980; *Muller and Raab*, 1997; *Vanorio et al.*, 2002; *Vinciguerra et al.*, 2005; *Wang et al.*, 1998; *Winkler and Murphy*, 1995]. Although *P* wave velocities and their variations cannot generally be interpreted uniquely, the spatial association of seismic velocity anomalies with known or inferred

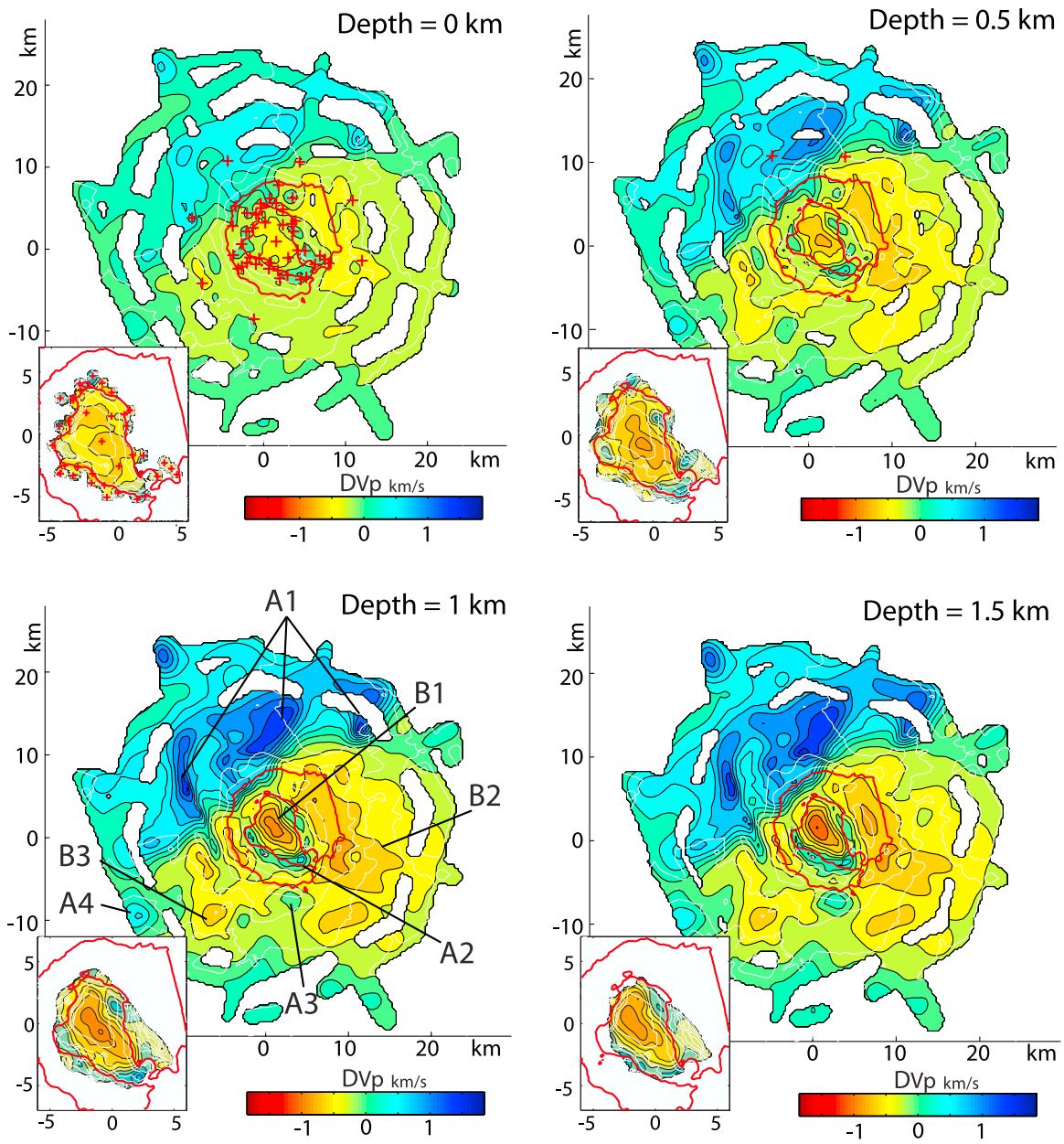

Figure 6. Horizontal slices through the final tomographic velocity model at several depths. Perturbations with respect to the starting model are contoured; contour interval 0.2 km/s. Insets show results of dense inversion within Port Foster. The coast of Deception Island is outlined in red; seismometer locations are red crosses. Areas with zero or low ray coverage are not shown. Arrows, see text for details.

geological structures may be used to understand the anomaly pattern of the tomographic image.

[31] The high-velocity region in the NW sector of Figure 6 (A1) represents the seismic image of the crystalline basement of the pre-Bransfield continental crust. It coincides in position and absolute velocity (4.0–5.5 km/s [*Christeson et al.*, 2003; *Grad et al.*, 1997]) with the SSI basement that is known to be close to the surface in this area. The crust to the SE of this region is within the Bransfield Basin and has markedly lower velocities (~1 km/s lower at the same depth) that are likely due to a thicker sediment layer. Other seismic studies have shown that the Bransfield Basin around Deception Island has undergone considerable extension, and the shallow crust is composed of sedimentary deposits of variable thickness and rotated fault blocks [*Barker and Austin*, 1998; *Gracia et al.*, 1996].

[32] We interpret the sharp, linear NE-SW trending boundary between the high- and low-velocity regions as the major fault zone that defines the northwestern limit of the Bransfield Basin. The position of this sharp lateral velocity variation (>0.8 km/s over a distance of 2–3 km (Figure 7)) coincides with a step in the bathymetry from the shallower SSI platform to the deeper Bransfield Basin floor, although near Deception Island the sense of this step is reversed (Figure 2 and *Barclay et al.* [2009]). This feature continues to the NE where it has been imaged by seismic reflection and refraction studies and interpreted as the footwall zone of a major normal fault system [*Barker and*

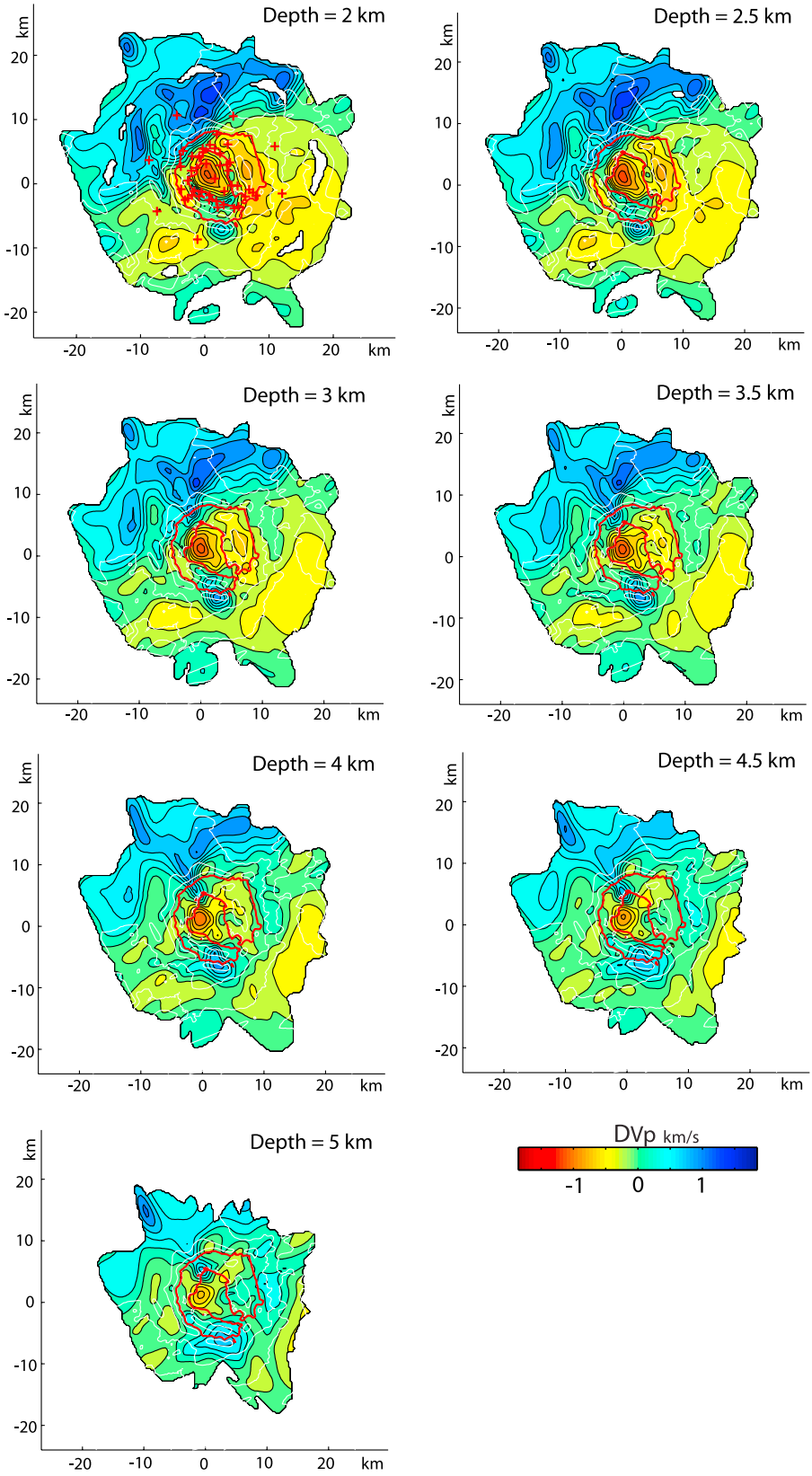

Figure 6. (continued)

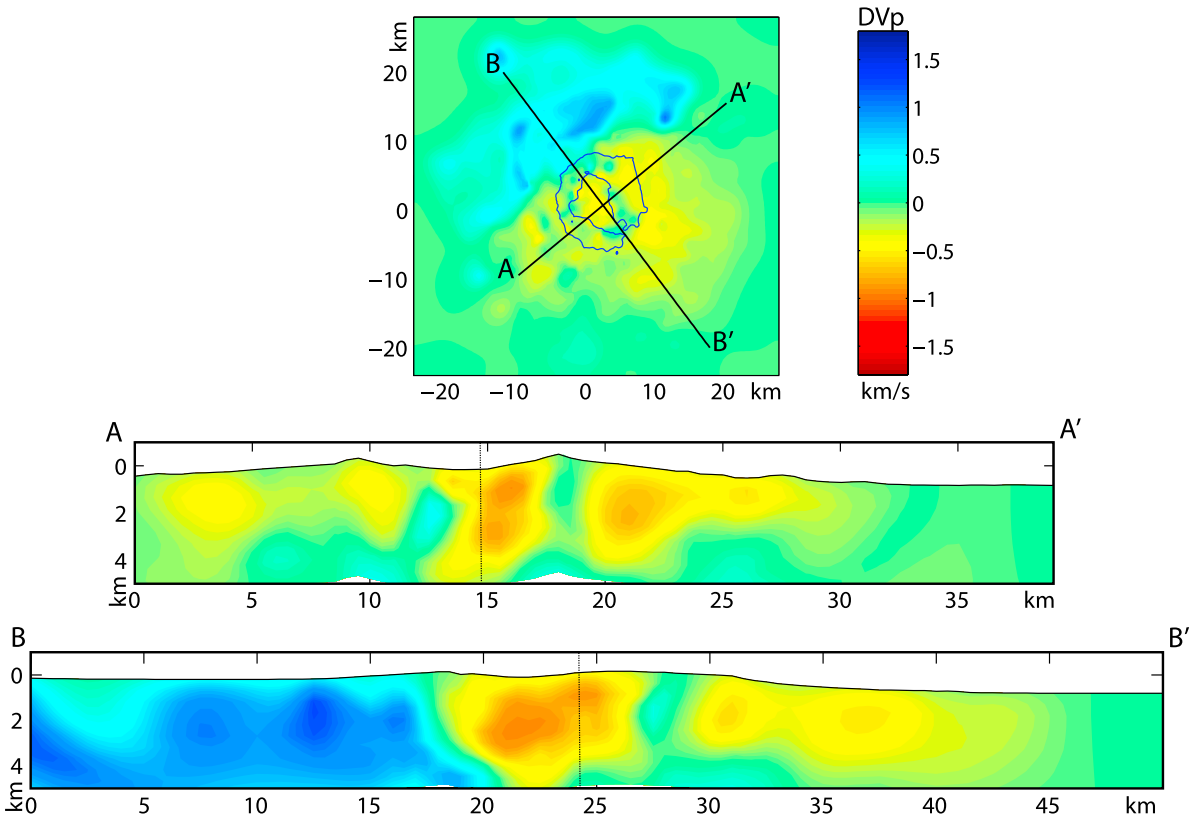

Figure 7. (top) The horizontal slice at 0 km depth through the final tomographic velocity model. (middle and bottom) Vertical slices through the same velocity model, along profiles indicated in Figure 7 (top) (AA′ and BB′). Perturbations with respect to the starting model are shown; depths are in km.

Austin, 1994; *Christeson et al.*, 2003; *Lawver et al.*, 1996]. Gravity and magnetic data are also consistent with the presence of a major fault zone [*Muñoz-Martin et al.*, 2005; *Navarro et al.*, 2002].

[33] The three velocity maxima that are superimposed on the high-velocity SSI platform are likely caused by areas of particularly shallow basement that are separated by two basins with relatively thicker sediment. This interpretation is supported by bathymetry data and seismic reflection data [*Barclay et al.*, 2009; *Barker and Austin*, 1998], at least for the two easternmost maxima. The positions of the three high-velocity regions also coincide with offsets in the otherwise linear boundary between the SSI platform and Bransfield Basin; the easternmost offset is apparent in the bathymetry as well. We apply the same interpretation to the westernmost anomaly, although this anomaly may be an artifact because its presence is controlled by a single line of shots, no seismic reflection lines cross this feature, and it has no bathymetric expression.

[34] The high-velocity anomalies we image on the SSI platform indicate the presence of large NW-SE trending structures. Although the primary tectonic fabric is NE-SW and parallel to the Bransfield Strait, there is considerable evidence for NW-SE trending fault systems in the vicinity of Deception Island. The entire continental upper crust of the Bransfield Basin is characterized by extensional horst-graben structures that are formed by NW-SE trending fault systems [*Barker and Austin*, 1998; *Gracia et al.*, 1996; *GRAPE Team*, 1990; *Prieto et al.*, 1998], and are possibly related to the southward distant propagation of the Hero Fracture Zone [*Rey et al.*, 1995; *Robertson-Maurice et al.*, 2003]. NW-SE oriented faults have been related to an offset in the Bransfield axial neovolcanic zone toward the South Shetland margin [*Christeson et al.*, 2003] and to the actual deformation pattern of Deception Island area [*Ramirez-Rodriguez*, 2006]. Additional evidence for NW-SE offsets comes from the Bouguer gravity anomaly map of *Muñoz-Martin et al.* [2005], where the alignment of gravity maxima is interrupted by a dextral strike slip fault that displaces the Livingstone Island basement toward the SE. In addition, *Ashcroft* [1972] notes in his seismic profiles the presence of a fault system across the SE coast of Livingston; *Grad et al.* [1992] model a strongly inclined basement reflector in the same location.

[35] The most pronounced low-velocity anomaly we image is located beneath the floor of Port Foster (B1). It extends to the maximum resolved depth of 5.5 km, and reaches its maximum velocity perturbation (∼2 km/s) with respect to the starting model between 1 km and 2 km depth (Figure 7). The shallowest 1.5 km of this anomaly is imaged in detail by the dense inversion. The presence of this low-velocity volume can be explained by the combination of two main different factors depending on the depth.

[36] At shallow depths, the anomaly is attributed to low-velocity sediments that likely derive from the fragmental volcanic products that have been formed throughout the entire volcanic history of the island [*Smellie et al.*, 2002] and that have been deposited in Port Foster by streams, ice

and mass wasting [*Inbar*, 1995]. At 0–0.5 km depth the anomaly includes several pronounced velocity lows, some of which coincide with the location of the 1967 and 1970 eruption deposits and present geothermal activity. Previous seismic studies also indicate the presence of a sedimentary layer [*Ashcroft*, 1972; *Grad et al.*, 1992; *Rey et al.*, 1995; *Somoza et al.*, 2004] which may be situated in a structural depression limited by NNE-SSW trending faults [*Saccorotti et al.*, 2001]. Seismic refraction experiments within Port Foster have modeled a ~1.2–1.4 km thick layer of 3.5 km/s underlain by a higher-velocity region of 4.5 km/s [*Grad et al.*, 1992; Ben-Zvi et al., presented paper, 2007]. This structure is in agreement with the absolute velocity of our velocity model for Port Foster, which is approximately 3 km/s between the surface and ~1.5 km depth, and is consistent with the presence of ash and other sedimentary deposits at various levels of compaction [*Ashcroft*, 1972; *Grad et al.*, 1992], and possibly a vigorous geothermal system [*Caselli et al.*, 2004; *Marti and Baraldo*, 1990].

[37] In depth, the amplitude and extension of the anomaly cannot be explained by a thicker layer of sediments alone, however, and requires high temperatures and partial melt, located beneath Port Foster at depths greater than 1–2 km [*Ben-Zvi et al.*, 2009]. The presence of a magma reservoir is supported by a number of previous studies. Shallowing of the floor of the northern subbasin of Port Foster, even if not recognized in the most recent surveys [*Barclay et al.*, 2009], has been attributed to a high sedimentation rate as well as magma influx at depth [*Cooper et al.*, 1999]. Magnetic anomalies show a minimum with a NNW-SSE trend, that is explained by the reduction of magnetization of volcanic intrusive rocks by shallow fluid circulation close to a deeper magma body [*Catalan et al.*, 2006; *García et al.*, 1997; *Muñoz-Martin et al.*, 2005; *Ortiz et al.*, 1992]. Changes in fumarole compositions observed in 1999 are also consistent with the emplacement of shallow magma in the area of Fumarole Bay [*Caselli et al.*, 2004]. Low seismic velocities and high seismic attenuation observed within Port Foster have also been explained as the existence of a hot magmatic intrusion [*Vila et al.*, 1992, 1995].

[38] The other low- and high-velocity anomalies in the tomographic image can be explained by a combination of thicker sedimentary deposits or volcanic extrusives and the presence of volcanic intrusive rocks, respectively. The large low-velocity region to the ESE of Deception Island (B2) corresponds to seafloor that is characterized by sediment transport (gullies, ridges and debris flows) from Deception Island into the Central Bransfield Basin [*Barclay et al.*, 2009]. Its overall shape is strongly irregular although the maximum perturbation at 0.5 km depth is aligned parallel to the island's strikingly linear eastern coast, Costa Recta. Several models have been proposed for the origin of this coastline including the footwall of an active normal fault [*Fernandez-Ibañez et al.*, 2005; *Maestro et al.*, 2007; *Smellie*, 2001]; down-dropping along this fault may have increased the sediment thickness. The other pronounced low-velocity region (B3) that is located to the SW of the island is associated with a rougher seafloor that includes a number of small seamounts and may be due to a thicker extrusive layer [*Barclay et al.*, 2009].

[39] We explain the other high-velocity anomalies in the image as intrusive or extrusive rocks that are surrounded by lower-velocity sediments. The low-velocity anomaly within Port Foster is partially surrounded by a horseshoe-shaped pattern of high velocities that approximately follows the coast and persists in our image between the surface and ~3 km depth (A2). These anomalies, which are in a particularly well resolved region, may either correspond to a precaldera shield phase of the ancient Deception Island, to a previous caldera rim, or to frozen, shallow level intrusions that may have fed earlier eruptions. The high-velocity anomaly that is directly to the south of Deception Island (A3) has the same size and location of an isolated Bouguer gravity and magnetization high [*Muñoz-Martin et al.*, 2005] and may represent a buried volcanic intrusion. We apply a similar interpretation to the high-velocity anomaly (A4) at about 20 km WSW from Port Foster, which is centered on Sail Rock, an eroded andesitic sea stack.

7. Discussion

[40] The nature of the seismic anomalies outlined above and their interpretation in a wider geodynamic context can constitute a tool to understand the evolution of a back arc basin and its role in the development of the local volcanism. Hence, those results help us to address several outstanding questions that arise in the study of similar tectonic settings.

[41] Figure 8 is a tentative representation of the regional tectonics based on our interpretation. It illustrates the main tectonic units and the processes that take place both at large scale and locally at Deception Island.

7.1. Deception Island Magmatism

[42] The main feature resolved by our seismic tomography experiment is the strong low-velocity volume beneath Port Foster that is interpreted as the combined presence of a shallow sedimentary cover and a deeper volume of partial melt. Imaging this magmatic system allows us to address the evolution and structure of the volcano, the interactions between volcanism and faulting, and the present seismic activity of the island.

[43] Although our data do not constrain the depth extent of this volume, seismic refraction and tomography profiles that cross Deception Island suggest that Port Foster is underlain by a ~1.2–1.4 km thick sedimentary layer above an extensive magma chamber that extends downward from ~2 km to at least 5 km depth. The low velocities may also be due to the presence of high temperatures, or altered or fractured rocks, but the magnitude of the anomaly is consistent with the presence of a significant volume of partial melt.

[44] The first seismological implication of this model concerns the distribution of the VT activity, located in the northern sector of Deception Island at shallow depth within Port Foster [*Alguacil et al.*, 1999; *Ibañez et al.*, 2003]. Similarly, seismic profiles of Port Foster indicate the absence of faulting in the middle of the bay [*Ashcroft*, 1972; *Grad et al.*, 1992]. Taken together, these observations point to ductile behavior of the hot, partially molten material below the shallower sedimentary levels.

[45] In addition, the LP seismic activity may also be related to the presence of shallow aquifers hosted by the pyroclastic layers and in contact with high-temperature rocks, with the circulation likely controlled by the local

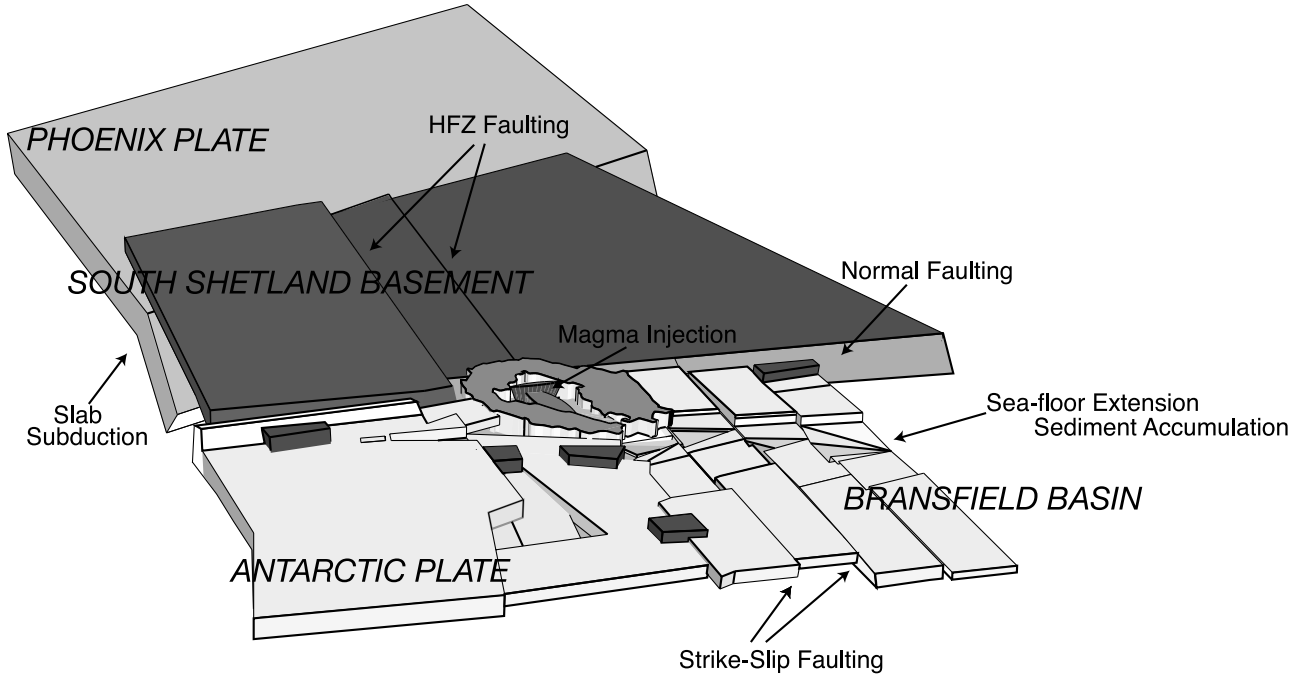

Figure 8. Sketch of Deception Island region. The names of the tectonic plates, main structural features (HFZ, Hero Fracture Zone), and ongoing processes are indicated. Dark areas represent crystalline blocks; inside Deception Island are magmatic injections. See text for details and interpretation.

fault system, around and across the bay [*Almendros et al.*, 1997].

[46] There are two major fault systems that cross Deception Island and that, by providing pathways for hydrothermal fluids and magma, may have influenced the distribution of volcanism and geothermal activity. The continuation of the faulted northern margin of the Central Bransfield Basin, which is present in our tomographic image as the major velocity contrast, that crosses the northwestern sector of Deception Island and has been mapped on the surface as several faults, coincides with the eruption centers of the 1967 and 1970 events and with the highest concentrations of As, Rb, Ba observed in the island [*Somoza et al.*, 2004]. In correspondence of Pendulum Cove and Fumarole Bay, several authors have recognized steeply dipping normal faults with a N40–N60 orientation [*De Rosa et al.*, 1995; *Gonzalez-Casado et al.*, 1999; *Maestro et al.*, 2007]. Other submarine fractures in this region also have a NE-SW direction [*Rey et al.*, 2002] and may be organized in graben-like structures across the bay [*Rey et al.*, 1997]. The volcano-tectonic seismic activity, which has a NE-SW orientation and normal mechanism [*Ibañez et al.*, 2003; *Vila et al.*, 1992] is also consistent with these fault zones.

[47] The other fault system that has been identified on Deception Island may also strongly influence the spatial distribution of volcanism, seismicity and hydrothermal activity. The NW-SE trending fracture system, which may be related to the southeastward extension of the Hero Fracture Zone may have influenced the location of some of the other eruptions at Deception Island (e.g., in 1969).

[48] The combined effect of these two recognized crustal actions may be responsible for the mixed nature of the magmatic products of Deception Island. The presence of different magmas has been well established and attributed to the regional extensional tectonics with scavenging of fractures [*Smellie et al.*, 2002].

7.2. Volcano-Earthquake Interactions

[49] Our results indicate that faulting has a strong influence on the spatial distribution of volcanic processes at Deception Island. In addition, we may refer to this model to address the evolution of the magmatic system in the context of the Bransfield Basin.

[50] The regional seismicity within the Bransfield Basin is strongly clustered around Deception and Bridgeman Islands, the two largest volcanoes [*Vuan et al.*, 2005]. However, no clear temporal relationships between earthquakes and volcanism at Deception Island have been established, primarily because of the difficulties of data collection at a remote site. Past eruptions are not or poorly documented and even today the island is only monitored seasonally. Typically only large regional earthquakes are located [*Ibañez et al.*, 1997; *Pelayo and Wiens*, 1989; *Robertson-Maurice et al.*, 2003; *Simkin et al.*, 1981; *Talandier and Okal*, 1987], while the smallest local events are only recognized and studied during seasonal campaigns.

[51] However, there is strong anecdotal evidence for preeruption earthquake activity for all of the most recent eruptions. The three last eruptions are documented mostly from the descriptions of researchers at the scientific bases and by old seismograms: (1) before the onset of the 1967 eruption (4 December 1967) some earthquakes were recorded at the British Antarctic Survey station on Deception Island, beginning late April 1967; (2) on 21 February 1969 the scientists of the scientific stations were shaken by what they reported as a "particularly strong earthquake" which was immediately followed by the erup-

tion; and (3) the eruption of 13 August 1970 was not directly observed, but the seismograph at the British Antarctic survey station on King George Island recorded an earthquake located near Deception Island.

[52] In seismic catalogs, the period between 1967 and 1970 is characterized by intense seismic activity [*Pelayo and Wiens*, 1989]. A group of earthquakes was strongly clustered around Deception Island during 1970 and occurred around the same time as the reported volcanic eruption. Other events in 1974 were aligned along a seismogenic zone extending NE-SW between Deception Island and Livingstone Island. Two major events, not followed by eruptions, on 8 February 1971 (magnitude $m_b = 6.3$) and on 13 December 1982 ($m_b = 5.8$) occurred to the SW of Deception Island, with the same alignment.

[53] In these cases, known eruptions were either preceded by or accompanied by earthquakes that were too powerful to be caused by the eruption itself. The earthquake locations appear to coincide with the sharp velocity contrast and major fault zone that separates the Bransfield Basin crust and the SSI platform [*Robertson-Maurice et al.*, 2003; *Vuan et al.*, 2005]. The occurrence of earthquakes in more competent crustal regions, with brittle behavior and high seismic velocity, has been widely discussed [*Lees and Malin*, 1990; *Zhao and Kanamori*, 1993]. In our case, the NW high velocity reasonably can be the most important seismogenetic zone in Deception Island.

[54] At Deception Island, this fault system is located only a few kilometers from the inferred magma body, and is associated with an extensional stress field that is favorable to magma upwelling. It is therefore likely that this fault system directly influences Deception Island volcanism. Regional seismicity can also cause volcanic unrest as a result of stress transfer [*Manga*, 2007; *Manga and Brodsky*, 2006; *Mellors et al.*, 2007; *Walter et al.*, 2007] and this process may also be important at Deception Island. Understanding stress triggering is important for the interpretation of precursors, early warning and hazard assessment, especially for a volcano such as Deception Island, which has a poorly understood eruptive history.

8. Conclusions

[55] The 3-D seismic *P* wave tomographic image of Deception Island volcano shows strong lateral velocity variations that are attributed to the presence of crustal magmatic systems with partial melt regions or frozen intrusive bodies, of sediment thickness variations and crustal bodies of different age and origin.

[56] A magma chamber of similar dimension and depth has been scarcely imaged by previous seismic tomography studies (see the comprehensive bibliographic review by *Ben-Zvi et al.* [2009]). In the case of Deception Island, the geometry of the experiment has allowed the resolution of a shallow and wide low-velocity anomaly that roughly corresponds to the magma chamber. In a general sense, our results corroborate the feasibility and utility of joint land/sea active source seismic tomography experiments at tectonically and volcanically active regions.

[57] Main results include the following: (1) The large high-velocity zone to the NW of Deception Island, with its southeastward displaced maxima, constitutes the seismic image of some continental crystalline blocks produced by fracturing of the ancient Antarctic Plate, before it fragmented into the South Shetland platform and the Antarctic Peninsula. (2) The low-velocity volume beneath Port Foster points to the existence of a wide region of partial melt, between the shallow sedimentary layer and unresolved depths, possibly >5 km. (3) The low velocities distributed around and irregularly across the island are the seismic image of deposits of sediments of volcanic origin, variously distributed and transported by modeling agents. (4) High-velocity anomalies within Deception Island are due to remnants of the ancient basaltic deposits, buried rims of caldera structures or shield phase roots from the early history of the volcano. (5) High-velocity anomalies far away from the island are the modeled image of frozen intrusive bodies and massive deposits.

[58] Our results demonstrate the complexity of the volcanic structure and the necessity of further research. The introduction of natural seismicity data may help to illuminate the deeper structure of Deception Island and may provide crucial information on actively deforming regions and the anisotropic properties of the crust, while focal mechanism studies can give constraints about the stress field distribution. The study of the Vp/Vs distribution might better constrain the inner structure and the action of fluid-related processes. Finally, the other volcanic centers within the Bransfield Basin are in many ways similar to Deception Island and may be useful analogs of Deception Island's early evolution.

[59] **Acknowledgments.** We are grateful to the officers and crew of the R/V *Hesperides* and R/V *Las Palmas*, the personnel of the Marine Technology Unit (UTM), and the members of the TOMODEC Working Group. Additional field support was provided by the Gabriel de Castilla base. This work was supported by the Spanish Education and Research Ministry grants REN 2001-3833, CGL2005-05789-C02-02/ANT, POL2006-08663, and CGL2008-01660 and the U.S. National Science Foundation grant ANT-0230094. The ocean bottom seismometers were provided by the U.S National Oceanographic Instrument Pool.

References

Alguacil, G., J. Almendros, E. Del Pezzo, A. García, J. M. Ibañez, M. La Rocca, J. Morales, and R. Ortiz (1999), Observations of volcanic earthquakes and tremor at Deception Island, Antarctica, *Ann. Geofis.*, *42*, 417–436.

Almendros, J., J. M. Ibañez, G. Alguacil, E. Del Pezzo, and R. Ortiz (1997), Array tracking of the volcanic tremor source at Deception island, Antarctica, *Geophys. Res. Lett.*, *24*, 3069–3072.

Almendros, J., E. Carmona, and J. Ibañez (2004), Precise determination of the relative wave propagation parameters of similar events using a small-aperture seismic array, *J. Geophys. Res.*, *109*, B11308, doi:10.1029/2003JB002930.

Ashcroft, W. A. (1972), Crustal structure of the South Shetland Islands and Bransfield Strait, *Sci. Rep. 66*, 43 pp., Br. Antarct. Surv., London.

Barclay, A. H., and W. S. D. Wilcock (2004), Upper crustal seismic velocity structure and microearthquake depths at the Endeavour Segment, Juan de Fuca Ridge, *Geochem. Geophys. Geosyst.*, *5*, Q01004, doi:10.1029/2003GC000604.

Barclay, A. H., D. R. Toomey, G. M. Purdy, and S. C. Solomon (1998), Seismic structure and magmatic accretionary processes at the Mid-Atlantic Ridge, 35°N, *J. Geophys. Res.*, *103*, 17,827–17,844, doi:10.1029/98JB01275.

Barclay, A. H., W. S. D. Wilcock, and J. M. Ibañez (2009), Tectonic and volcanic influences at Deception Island, South Shetland Islands, *Antarct. Sci.*, *21*(2), 153–167, doi:10.1017/S0954192008001673.

Barker, D. H. N., and J. A. Austin (1994), Crustal diapirism in Bransfield Strait, West Antarctica: Evidence for distributed extension in marginal-basin formation, *Geology*, *22*, 657–660, doi:10.1130/0091-7613(1994)022<0657:CDIBSW>2.3.CO;2.

Barker, D. H. N., and J. A. Austin (1998), Rift propagation, detachment faulting, and associated magmatism in Bransfield Strait, Antarctic Peninsula, *J. Geophys. Res.*, *103*, 24,017–24,043, doi:10.1029/98JB01117.

Ben-Zvi, T., W. S. D. Wilcock, A. H. Barclay, D. Zandomeneghi, J. M. Ibañez, J. Almendros, and T. W. Group (2007), The P-wave velocity structure of Deception Island, Antarctica, from two-dimensional seismic tomography, in *Antarctica: A Keystone in a Changing World—Online Proceedings for the 10th International Symposium on Antarctic Earth Sciences*, edited by A. Cooper, C. Raymond, and the 10th ISAES Editorial Team, *U.S. Geol. Surv. Open File Rep.*, *2007-1047*, EA 078.

Ben-Zvi, T., W. S. D. Wilcock, A. H. Barclay, D. Zandomeneghi, J. M. Ibañez, and J. Almendros (2009), The *P* wave velocity structure of Deception Island, Antarctica, from two-dimensional seismic tomography: Evidence for a shallow magma chamber, *Antarct. Sci.*, *180*, 67–80.

Bird, P. (2003), An updated digital model of plate boundaries, *Geochem. Geophys. Geosyst.*, *4*(3), 1027, doi:10.1029/2001GC000252.

Bonner, B., J. Robert, A. Duba, and P. Kasameyer (1998), Laboratory studies of geyser rock and impacts on exploration, *Sci. Rep. UCRL-JC-131340*, Lawrence Livermore Natl. Lab., Livermore, Calif.

Caselli, A. T., M. Santos-Afonso, and M. R. Agusto (2004), Gases fumarolicos de la isla Decepcion (Shetland del Sur, Antartida): Variaciones quimicas y depositos vinculados a la crisis sismica de 1999, *Asoc. Geol. Argent. Rev.*, *59*, 291–302.

Catalan, M., L. M. Agudo, and A. Muñoz-Martin (2006), Geomagnetic secular variation of Bransfield Strait (western Antarctica) from analysis of marine crossover data, *Geophys. J. Int.*, *165*, 73–86, doi:10.1111/j.1365-246X.2006.02877.x.

Chouet, B. A. (2003), Volcano seismology, *Pure Appl. Geophys.*, *160*, 739–788, doi:10.1007/PL00012556.

Christensen, N. I. (1996), Poisson's ratio and crustal seismology, *J. Geophys. Res.*, *101*, 3139–3156, doi:10.1029/95JB03446.

Christeson, G. L., D. H. N. Barker, J. A. Austin Jr., and I. W. D. Dalziel (2003), Deep crustal structure of Bransfield Strait: Initiation of a back arc basin by rift reactivation and propagation, *J. Geophys. Res.*, *108*(B10), 2492, doi:10.1029/2003JB002468.

Cooper, A. P. R., J. L. Smellie, and J. Maylin (1999), Evidence for shallowing and uplift from bathymetric records of Deception Island, Antarctica, *Antarct. Sci.*, *10*, 455–461.

Creager, K. C., and L. M. Dorman (1982), Location of instruments on the seafloor by joint adjustments of instruments and ship positions, *J. Geophys. Res.*, *87*, 8379–8388, doi:10.1029/JB087iB10p08379.

De Rosa, R., R. Mazzuoli, R. H. Omarini, G. Ventura, and J. G. Viramonte (1995), A volcanological model for the historical eruptions at Deception Island (Bransfield Strait, Antarctica), *Terra Antarct.*, *2*, 95–101.

Dietrich, R., R. Dach, G. Engelhardt, J. Ihde, W. Korth, and H.-J. Kutterer (2001), ITRF coordinates and plate velocities from repeated GPS campaigns in Antarctica—An analysis based on different individual solutions, *J. Geod.*, *74*, 756–766, doi:10.1007/s001900000147.

Dunn, R. A., D. R. Toomey, R. Detrick, and W. S. D. Wilcock (2001), Continuous mantle melt supply beneath an overlapping spreading center on the East Pacific Rise, *Science*, *291*, 1955–1958, doi:10.1126/science.1057683.

Evangelidis, C. P., T. A. Minshull, and T. J. Henstock (2004), Three-dimensional crustal structure of Ascension Island from active source seismic tomography, *Geophys. J. Int.*, *159*, 311–325, doi:10.1111/j.1365-246X.2004.02396.x.

Fehler, M., L. House, W. Scott-Phillips, and R. Potter (1998), A method to allow temporal variation of velocity in travel-time tomography using microearthquakes induced during hydraulic fracturing, *Tectonophysics*, *289*, 189–201, doi:10.1016/S0040-1951(97)00315-6.

Fernandez-Ibañez, F., R. Perez-Lopez, J. J. Martinez-Diaz, C. Paredes, J. L. Giner-Robles, A. T. Caselli, and J. M. Ibañez (2005), Costa Recta beach, Deception Island, West Antarctica: A retreated scarp of a submarine fault?, *Antarct. Sci.*, *17*, 418–426, doi:10.1017/S0954102005002841.

Galindo-Zaldivar, J., A. Jabaloy, A. Maldonado, and C. S. de Galdeano (1996), Continental fragmentation along the South Scotia Ridge transcurrent plate boundary (NE Antarctic Peninsula), *Tectonophysics*, *258*, 275–301, doi:10.1016/0040-1951(95)00211-1.

García, A., I. Blanco, J. M. Torta, M. M. Astiz, J. M. Ibáñez, and R. Ortiz (1997), A search for the volcanomagnetic signal at Deception volcano (South Shetland I., Antarctica), *Ann. Geofis.*, *40*, 319–327.

Goldstein, P., D. Dodge, M. Firpo, and L. Minner (2003), SAC2000: Signal processing and analysis tools for seismologists and engineers, in *International Handbook of Earthquake and Engineering Seismology, Part B*, *Int. Geophys. Ser.*, vol. 81B, edited by W. Lee et al., p. 85.5, Academic, London.

Gonzalez-Casado, J. M., J. Lopez-Martinez, J. Giner, J. J. Duran, and P. Gumiel (1999), Analisis de la microfracturacion en la Isla Decepcion, Antartida Occidental, *Geogaceta*, *26*, 27–30.

Gordon, A. L., and W. D. Nowlin (1978), Basin waters of Bransfield Strait, *J. Phys. Oceanogr.*, *8*, 258–264, doi:10.1175/1520-0485(1978)008<0258:TBWOTB>2.0.CO;2.

Gracia, E., M. Canals, M. L. Farran, M. J. Prieto, and J. Sorribas (1996), Morphostructure and evolution of the central and eastern Bransfield basins (NW Antarctic Peninsula), *Mar. Geophys. Res.*, *18*, 429–448, doi:10.1007/BF00286088.

Grad, M., A. Guterch, and P. Sroda (1992), Upper crustal structure of Deception Island area, Bransfield Strait, West Antarctica, *Antarct. Sci.*, *4*, 469–476, doi:10.1017/S0954102092000683.

Grad, M., H. Shiobara, T. Janik, A. Guterch, and H. Shimamura (1997), Crustal model of Bransfield Rift, West Antarctica, from detailed OBS refraction experiments, *Geophys. J. Int.*, *130*, 506–518, doi:10.1111/j.1365-246X.1997.tb05665.x.

GRAPE Team (1990), Preliminary results of seismic reflection investigations and associated geophysical studies in the area of the Antarctic Peninsula, *Antarct. Sci.*, *2*, 223–234.

Ibañez, J. M., J. Morales, G. Alguacil, J. Almendros, R. Ortiz, and E. Del Pezzo (1997), Intermediate-focus earthquakes under South Shetland Island (Antarctica), *Geophys. Res. Lett.*, *24*, 531–534, doi:10.1029/97GL00314.

Ibañez, J., P. Morales, G. Alguacil, J. Almendros, R. Ortiz, M. Del Pezzo, E. La Rocca, and A. Garcia (2000), Seismovolcanic signals at Deception Island volcano, Antarctica: Wave field analysis and source modeling, *J. Geophys. Res.*, *105*, 13,905–13,931, doi:10.1029/2000JB900013.

Ibañez, J. M., E. Carmona, J. Almendros, G. Saccorotti, E. Del Pezzo, M. Abril, and R. Ortiz (2003), The 1998–1999 seismic series at Deception Island volcano, Antarctica, *J. Volcanol. Geotherm. Res.*, *128*, 65–88, doi:10.1016/S0377-0273(03)00247-6.

Inbar, M. (1995), Fluvial morphology and streamflow on Deception Island, Antarctica, *Geogr. Ann.*, *77*, 221–230, doi:10.2307/521331.

Keller, R. A., M. R. Fisk, J. L. Smellie, J. A. Strelin, and L. A. Lawver (2002), Geochemistry of back arc basin volcanism in Bransfield Strait, Antarctica: Subducted contributions and along-axis variations, *J. Geophys. Res.*, *107*(B8), 2171, doi:10.1029/2001JB000444.

Klepeis, K. A., and L. A. Lawer (1996), Tectonics of the Antarctic-Scotia plate boundary near Elephant and Clarence Islands, West Antarctica, *J. Geophys. Res.*, *101*, 20,211–20,231, doi:10.1029/96JB01510.

Lawver, L. A., B. J. Sloan, D. H. N. Barker, M. Ghidella, R. P. Von Herzen, R. A. Keller, G. P. Klinkhammer, and C. S. Chin (1996), Distributed, active extension in Bransfield Basin, Antarctic Peninsula: Evidence from multibeam bathymetry, *GSA Today*, *6*, 1–6.

Lees, J. M. (2007), Seismic tomography of magmatic systems, *J. Volcanol. Geotherm. Res.*, *167*, 37–56, doi:10.1016/j.jvolgeores.2007.06.008.

Lees, J. M., and P. E. Malin (1990), Tomographic images of P wave velocity variation at Parkfield, California, *J. Geophys. Res.*, *95*, 21,793–21,804, doi:10.1029/JB095iB13p21793.

Lees, J. M., and H. Wu (2000), Poisson's ratio and porosity at Coso geothermal area, California, *J. Volcanol. Geotherm. Res.*, *95*, 157–173, doi:10.1016/S0377-0273(99)00126-2.

Maestro, A., L. Somoza, J. Rey, J. Martinez-Frias, and J. Lopez-Martinez (2007), Active tectonics, fault patterns, and stress field of Deception Island: A response to oblique convergence between the Pacific and Antarctic plates, *J. South Am. Earth Sci.*, *23*, 256–268, doi:10.1016/j.jsames.2006.09.023.

Manga, M. (2007), Did an earthquake trigger the May 2006 eruption of the Lusi mud volcano?, *Eos Trans. AGU*, *88*(18), 201, doi:10.1029/2007EO180009.

Manga, M., and E. Brodsky (2006), Seismic triggering of eruptions in the far field: volcanoes and geysers, *Annu. Rev. Earth Planet. Sci.*, *34*, 263–291, doi:10.1146/annurev.earth.34.031405.125125.

Marti, J., and A. Baraldo (1990), Pre-caldera pyroclastic deposits of Deception Island (South Shetland Islands), *Antarct. Sci.*, *2*, 345–352, doi:10.1017/S0954102090000475.

Marti, J., J. Vila, and J. Rey (1996), Deception Island (Bransfield Strait, Antarctica): An example of volcanic caldera developed by extensional tectonics, in *Volcanic Instability on the Earth and Other Planets*, edited by W. J. McGuire et al., *Geol. Soc. Spec. Publ.*, vol. 110, pp. 253–265.

Mavko, G. M. (1980), Velocity and attenuation in partially molten rocks, *J. Geophys. Res.*, *85*, 5173–5189, doi:10.1029/JB085iB10p05173.

Mellors, R., D. Kilb, A. Aliyev, A. Gasanov, and G. Yetirmishli (2007), Correlations between earthquakes and large mud volcano eruptions, *J. Geophys. Res.*, *112*, B04304, doi:10.1029/2006JB004489.

Moser, T. J. (1991), Shortest path calculation of seismic rays, *Geophysics*, *56*, 59–67, doi:10.1190/1.1442958.

Muller, H. J., and S. Raab (1997), Elastic wave velocity of granite at experimental simulated partial melting conditions, *Phys. Chem. Earth*, *22*, 93–96, doi:10.1016/S0079-1946(97)00084-0.

Muñoz-Martin, A., M. Catalan, J. Martin, and A. Carbo (2005), Upper crustal structure of Deception Island area (Bransfield Strait, Antarctica)

from gravity and magnetic modelling, *Antarct. Sci.*, *17*, 213–224, doi:10.1017/S0954102005002622.

Navarro, F. J., E. J. Velez, A. G. Camacho, and R. Vieira (2002), A gravity survey of Deception Island (South Shetland Islands, Antarctica), in *Antarctica at the Close of a Millennium*, edited by J. A. Gamble et al., *R. Soc. N. Z. Bull.*, vol. 35, 515–523.

Ortiz, R. (1997), Monitoring of the volcanic activity of Deception Island, South Shetland Islands, Antarctica (1986–1995), in *Antarctic Region: Geological Evolution and Processes*, edited by C. A. Ricci, pp. 1071–1076, Terra Antarct., Siena, Italy.

Ortiz, R., J. Vila, A. Garcia, A. G. Camacho, J. L. Diez-Gil, A. Aparicio, R. Soto, and J. G. Viramonte (1992), Geophysical features of Deception, in *Recent Progress in Antarctic Earth Sciences*, edited by Y. Yoshida et al., pp. 443–448, Terra Sci., Tokyo.

Paige, C. C., and M. A. Saunders (1982), LSQR: An algorithm for sparse linear equations and sparse least squares, *Trans. Math. Software*, *8*, 43–71, doi:10.1145/355984.355989.

Paredes, C., R. Perez-Lopez, J. L. Giner-Robles, R. de la Vega, A. Garcia-Garcia, and P. Gumiel (2006), Distribucion espacial y zonificacion tectonica de los morfolineamentos en la Isla Decepcion (Shetland del Sur, Antartida), *Geogaceta*, *39*, 75–78.

Pelayo, A. M., and D. A. Wiens (1989), Seismotectonic and relative plate motions in the Scotia Sea region, *J. Geophys. Res.*, *94*, 7293–7320, doi:10.1029/JB094iB06p07293.

Prieto, M. J., M. Canals, G. Ercilla, and M. de Batist (1998), Structure and geodynamic evolution of the Central Bransfield Basin (NW Antarctica) from seismic reflection data, *Mar. Geol.*, *149*, 17–38, doi:10.1016/S0025-3227(98)00038-3.

Ramirez-Rodriguez, M. E. (2006), *Modelización de la deformación superficial en areas volcanicas mediante la teoria de wavelets. Aplicacion al volcan Decepción*, 264 pp., Universidad de Cadiz, Cadiz, Spain.

Rey, J., L. Somoza, and J. Martinez-Frias (1995), Tectonic, volcanic and hydrothermal event sequence on Deception Island (Antarctica), *Geo Mar. Lett.*, *15*, 1–8, doi:10.1007/BF01204491.

Rey, J., L. Somoza, J. Martínez-Frias, R. Benito, and S. Martín-Alfageme (1997), Deception Island (Antarctica): A new target for exploration of Fe-Mn mineralization?, in *Manganese Mineralization: Geochemistry and Mineralogy of Terrestrial and Marine Deposits*, edited by K. Nicholeson et al., *Geol. Soc. Spec. Publ.*, 119, 239–251.

Rey, J., A. Maestro, L. Somoza, and J. L. Smellie (2002), Submarine morphology and seismic stratigraphy of Port Foster, in *Geology and Geomorphology of Deception Island*, edited by J. L. Smellie and J. López-Martínez, pp. 40–46, Br. Antarct. Surv, Cambridge, U. K.

Robertson-Maurice, S. D., D. A. Wiens, P. J. Shore, E. Vera, and L. M. M. Dorman (2003), Seismicity and tectonics of the South Shetland Islands and Bransfield Strait from a regional broadband seismograph deployment, *J. Geophys. Res.*, *108*(B10), 2461, doi:10.1029/2003JB002416.

Saccorotti, G., J. Almendros, E. Carmona, J. M. Ibañez, and E. Del Pezzo (2001), Slowness anomalies from two dense seismic arrays at Deception Island Volcano, Antarctica, *Bull. Seismol. Soc. Am.*, *91*, 561–571, doi:10.1785/0120000073.

Simkin, T., and L. Siebert (2002), *Global Volcanism Program*, Smithsonian Inst., Washington, D. C.

Simkin, T., L. Siebert, L. McClelland, D. Bridge, and L. Newhall (1981), *Volcanoes of the World*, 232 pp., Hutchinson Ross., Stroudsburg, Pa.

Smellie, J. L. (2001), Lithostratigraphy and volcanic evolution of Deception Island, South Shetland Islands, *Antarct. Sci.*, *13*, 188–209, doi:10.1017/S0954102001000281.

Smellie, J. L., J. Lopez-Martinez, and J. W. Thomson (2002), *Geology and Geomorphology of Deception Island*, British Antarct. Surv., Cambridge, U. K.

Somoza, L., J. Martinez-Frias, J. L. Smellie, J. Rey, and A. Maestro (2004), Evidence for hydrothermal venting and sediment volcanism discharged after recent short-lived volcanic eruptions at Deception Island, Bransfield Strait, Antarctica, *Mar. Geol.*, *203*, 119–140, doi:10.1016/S0025-3227(03)00285-8.

Talandier, J., and E. A. Okal (1987), Seismic detection of underwater volcanism: The example of French Polynesia, *Pure Appl. Geophys.*, *125*, 919–950, doi:10.1007/BF00879361.

Tian, T., S. D. Wilcock, D. R. Toomey, and R. S. Detrick (2000), Seismic heterogeneity in the upper crust near the 1991 eruption site on the East Pacific Rise, 9°50′N, *Geophys. Res. Lett.*, *27*, 2369–2372, doi:10.1029/1999GL011191.

Toomey, D. R., S. C. Solomon, and G. M. Purdy (1994), Tomographic imaging of the shallow crustal structure of the East Pacific Rise at 9 30′N, *J. Geophys. Res.*, *99*, 24,135–24,157, doi:10.1029/94JB01942.

Toomey, D. R., W. S. D. Wilcock, S. C. Solomon, W. C. Hammond, and J. A. Orcutt (1998), Mantle seismic structure beneath the MELT region of the East Pacific Rise from *P* and *S* wave tomography, *Science*, *280*, 1224–1227, doi:10.1126/science.280.5367.1224.

Toomey, D. R., D. Jousselin, R. A. Dunn, W. S. D. Wilcock, and R. S. Detrick (2007), Skew of mantle upwelling beneath the East Pacific Rise governs segmentation, *Nature*, *446*, 409–414, doi:10.1038/nature05679.

Vanorio, T., M. Prasad, D. Patella, and A. Nur (2002), Ultrasonic velocity measurements in volcanic rocks: Correlation with microtexture, *Geophys. J. Int.*, *149*, 22–36, doi:10.1046/j.0956-540x.2001.01580.x.

Vila, J., J. Marti, R. Ortiz, A. Garcia, and A. M. Correig (1992), Volcanic tremors at Deception Island (South Shetland Islands, Antarctica, *J. Volcanol. Geotherm. Res.*, *53*, 89–102, doi:10.1016/0377-0273(92)90076-P.

Vila, J., A. M. Correig, and J. Marti (1995), Attenuation and source parameters at Deception Island (South Shetland Islands, Antarctica), *Pure Appl. Geophys.*, *144*, 229–250, doi:10.1007/BF00878633.

Vinciguerra, S., C. Trovasto, P. G. Meredith, and P. M. Benson (2005), Relating seismic velocities, thermal cracking and permeability in Mt. Etna and Iceland basalts, *Int. J. Rock Mech. Min. Sci.*, *42*, 900–910, doi:10.1016/j.ijrmms.2005.05.022.

Vuan, A., S. D. Robertson Maurice, D. A. Wiens, and G. F. Panza (2005), Crustal and upper mantle S-wave velocity structure beneath the Bransfield Strait (West Antarctica) from regional surface, *Tectonophysics*, *397*, 241–259, doi:10.1016/j.tecto.2004.12.011.

Walter, T. R., R. Wang, M. Zimmer, H. Grosser, B. Luhr, and A. Ratdomopurbo (2007), Volcanic activity influenced by tectonic earthquakes: Static and dynamic stress triggering at Mt. Merapi, *Geophys. Res. Lett.*, *34*, L05304, doi:10.1029/2006GL028710.

Wang, Z., M. E. Cates, and R. T. Langan (1998), Seismic monitoring of a CO_2 flood in a carbonate reservoir: A rock physics study, *Geophysics*, *63*, 1604–1617, doi:10.1190/1.1444457.

Webb, S. C. (1998), Broad seismology and noise under the ocean, *Rev. Geophys.*, *36*, 105–142, doi:10.1029/97RG02287.

Winkler, K. W., and W. F. Murphy (1995), Acoustic velocity and attenuation in porous rocks, in *Rock Physics and Phase Relations: A Handbook of Physical Constants*, *AGU Ref. Shelf Ser.*, vol. 3, edited by T. J. Aherens, pp. 20–34, AGU, Washington, D. C.

Zhao, D., and H. Kanamori (1993), The1992 Landers earthquake sequence: Earthquake occurrence and structural heterogeneities, *Geophys. Res. Lett.*, *20*, 1083–1086, doi:10.1029/93GL01239.

J. Almendros and J. M. Ibañez Godoy, Instituto Andaluz de Geofísica, University of Granada, Campus de Cartuja s/n, E-18071 Granada, Spain.

A. Barclay, Lamont-Doherty Earth Observatory, Earth Institute at Columbia University, 61 Route 9W, Palisades, NY 10964, USA.

T. Ben-Zvi and W. S. D. Wilcock, School of Oceanography, University of Washington, Box 357940, Seattle, WA 98195-7940, USA.

D. Zandomeneghi, Department of Earth and Environmental Science, New Mexico Institute of Mining and Technology, 801 Leroy Place, Socorro, NM 87801, USA. (daria@ees.nmt.edu)